HOT LOOP OSCILLATIONS SEEN BY SUMER: EXAMPLES AND STATISTICS

T. J. Wang, S. K. Solanki, W. Curdt, D. E. Innes, and I. E. Dammasch
Max-Planck-Institut für Aeronomie, 37191 Katlenburg-Lindau, Germany

ABSTRACT

We measure physical parameters of Doppler-shift oscillations in 17 flare-like events. These events have been recorded by the Solar Ultraviolet Measurements of Emitted Radiation (SUMER) spectrometer on SOHO, along a slit fixed above limb active regions. The selected spectral windows contain emission lines with formation temperatures from $\sim 10^4$ to 10^7 K. The events were only detected in hot flare lines, without any signature in lines formed around 2×10^6 K. Similarly, the Doppler shift oscillations occur in regions coincident with hot soft X-ray loops, but not with EUV loops. The oscillations have periods of 11−31 min, with an exponential decay time of 5.5−29 min, and show an initial large shift pulse with peak velocities up to 200 km s^{-1}. Several indications suggest that the Doppler oscillations are incompressible coronal loop oscillations, that are usually excited impulsively by weak flare (or microflare) events that also produced a strong emission increase at $5-8\times10^6$ K.

Key words: solar flares; coronal oscillations; UV radiation, X-rays.

1. INTRODUCTION

Transverse oscillations of active region loops were first discovered with TRACE in EUV bands (Aschwanden et al., 1999), and more cases have been reported in a recent statistical study by Schrijver, Aschwanden & Title (2002) and Aschwanden et al. (2002). These transverse loop oscillations are excited by flares, and show a very quick decay on time scales of 3−21 min, with oscillation periods of 2−11 min. Aschwanden et al. (1999) and Nakariakov et al. (1999) have interpreted the loop oscillation as a fundamental resonance of the kink mode, and Nakariakov et al. (1999) concluded that the rapid damping is due to anomalously high viscosity, or resistivity in the coronal plasma. Ofman & Aschwanden (2002) investigated the scaling of the oscillation damping time for the TRACE loops, and found that the scaling agrees best with phase mixing as the damping mechanism.

Recently, additional evidence of damped oscillating coronal loops was found by SUMER spectral observations (Kliem et al., 2002; Wang et al., 2002a,b). They show that Doppler shift oscillations in hot coronal loops ($T \sim 10^7 K$) have a damping time range comparable to that of the TRACE loops, but oscillation periods distinctly longer than those observed by TRACE. This difference is confirmed by new observations with a higher cadence reported in this study. We present three typical case studies and statistical results of hot loop oscillations.

2. OBSERVATIONS AND DATA REDUCTION

In all cases, the SUMER spectrometer slit was placed at a fixed position in the corona about 100″ above an active region at the limb. The earlier observations during 1999−2001 were made in a wide spectral window with a 162 s exposure time. The new observations obtained in April 2002 were made in three lines (Si III/S III, Ca X, and Fe XIX) with a high cadence of 50 s.

After processing the raw data following standard procedures, a single Gaussian was fit to the lines to obtain a Doppler shift time series at each spatial pixel. Examples are shown in Figures 1 and 3. These exhibit distinct regions of coherent oscillations along the slit. For each region, we average over a width of 11 pixels (∼ 1″/pix) for the old data sets and 6 pixels for the new data sets to get its average time profile. The function

$$V(t) = V_0 + V_m sin(\omega t + \phi)e^{-\lambda t}, \qquad (1)$$

is then fit to the oscillation, where V_0 is the post-event Doppler shift, V_m is the shift amplitude and ω, ϕ, and λ are the frequency, phase, and decay rate of the oscillations. The parameters of the time series are listed in Table 1.

Proc. 'SOLMAG: Magnetic Coupling of the Solar Atmosphere Euroconference and IAU Colloquium 188' Santorini, Greece, 11-15 June 2002 (ESA SP-505, October 2002)

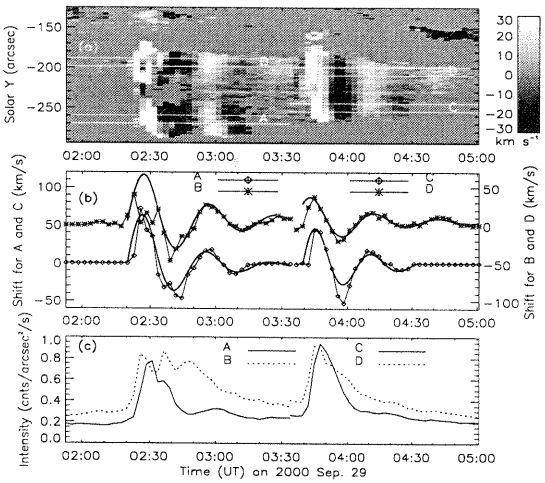

Figure 1. (a) Doppler-shift time series in the Fe XIX line on 29 Sep 2000, during 02:00–05:00 UT. (b) Time profiles of Doppler shifts for cuts A, B, C and D, averaged along the slit. The thick solid curves are the best fits employing function (1). (c) Average time profiles of line-integrated intensity for the four cuts shown in Fig. 1a.

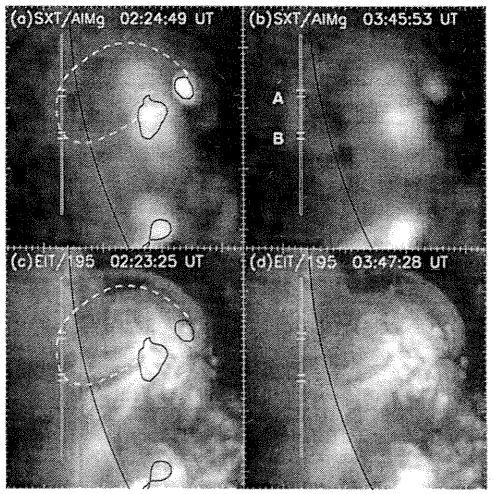

Figure 2. Overlay of the 4″ × 300″ SUMER slit on Yohkoh/SXT images (a and b), and on SOHO/EIT images (c and d). The dashed line and solid contours in (a) and (c) outline the SXT loop and brightenings, respectively. The positions A and B from Fig. 1a are indicated.

3. RESULTS: INDIVIDUAL EVENTS

3.1. Case 1: 9 March 2001

This is probably the clearest example of loop oscillations in our data set. Wang et al. (2002a,b) showed that the two similar Doppler oscillation events occurred within an interval of less than 2 hours, at the place coincident with a SXT loop. They found that the period for a standing slow mode, $2L/c_s = 15.8$ min, in agreement with the observed 14–18 min periods, but the absence of brightness fluctuations with the wave period argues against a compressible wave. On the other hand, an unusual coronal loop environment ($\beta \sim 2$) is implied if we interpret the Doppler oscillation as a standing kink mode.

3.2. Case 2: 29 September 2000

In this case, available coordinated observations between SUMER and Yohkoh/SXT provide convincing evidence that the Doppler oscillation corresponds to hot coronal loop oscillations. Wang et al. (2002a) showed that the SUMER time series revealed 4 hot plasma events. The two earlier events (Fig. 1) have well defined oscillations that coincide with the region where the slit crosses a large SXT loop (Fig. 2). EIT loops differ in position from the SXT loop. The later two events (10:17 UT and 13:13 UT) were both associated with GOES C-class flares, showing X-ray plasma ejections (Fig. 6 in Wang et al., 2002a). Slow mode standing waves have a period $\sim$ 40 min, assuming a sound speed of $c_s = 295$ km s^{-1}, for a loop length of $L \approx 356$ Mm, which is the length of the large loop system as measured from Figure 2a. This is 1.3–1.6 times the measured periods. We obtain $\beta \sim 1$ when the global kink mode is assumed.

3.3. Case 3: 11 April 2002

This is the best example showing Doppler oscillations in the new observations. Figure 3 shows that three oscillation events occurred within 2 hours, with the periods in the range of 13–18 min, similar to the previous results. The high cadence observations reveal propagation (phase delay) of Doppler disturbances along the slit. The disturbance from C to B (cut 1) and that from C to D (cut 2) have durations of 150 s and 200 s, so that this initial phase delay was not detectable in the previous low-cadence observations. The phase propagating speeds decrease with time. We measure the speed for CB as 96, 49, and 34 km s^{-1} from the slopes of cuts 1, 3 and 5, while the speed for CD is 83, 48, and 13 km s^{-1} from cuts 2, 4 and 6. Figures 3c and e show also distinctly different spatial distributions along the slit (e.g. at B, C, and D) in intensity and line width.

4. STATISTICAL RESULTS

We analyzed the 35 Doppler oscillation components in 17 flux enhancement events of hot plasma (> 6 MK). In each event, we identified several oscillation components along the slit, due to differences in Doppler shift, intensity, or line width. All events show the flux variations of flare-like impulsive profiles, but only 3 of the 17 events were associated with GOES flares. The histograms of physical parameters of the oscillations listed in Table 1 are shown in Figures 4 and 5. Although the new observations

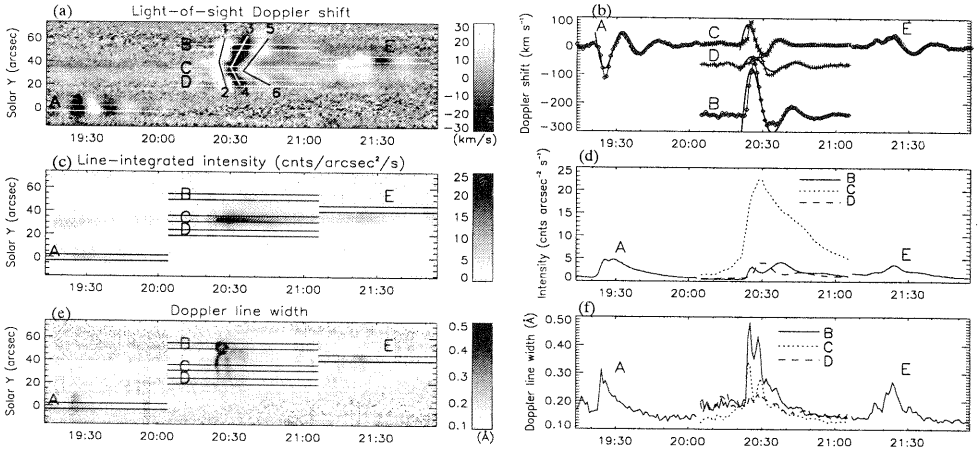

Figure 3. (a)Doppler-shift time series in the Fe XIX line on 11 Apr 2002. (b) Average time profiles of Doppler shifts for the cuts in (a) and their best fit curves. (c) Line-integrated intensity time series, and (d) the corresponding time profiles for the cuts. (e) Line width time series, and (f) the corresponding time profiles for the cuts.

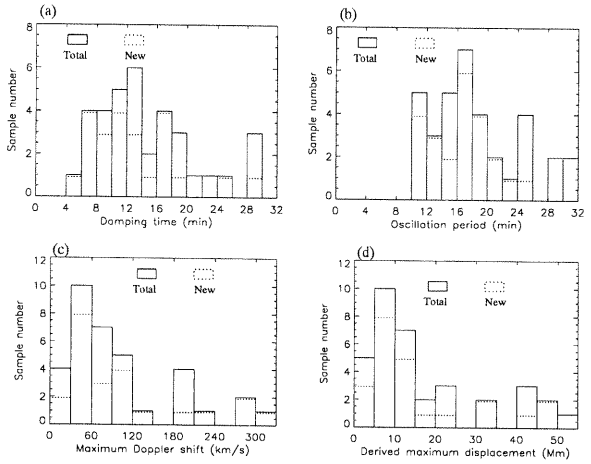

Figure 4. Histograms of (a) the damping time, (b) the oscillation period, (c) the maximum Doppler shift, and (d) the derived maximum displacement. The solid strips represent the total sample, including the data obtained in 1999-2001 with a low cadence of 162 s and the new data obtained in 2002 with a high cadence of 50 s. The dashed strips represent the new samples.

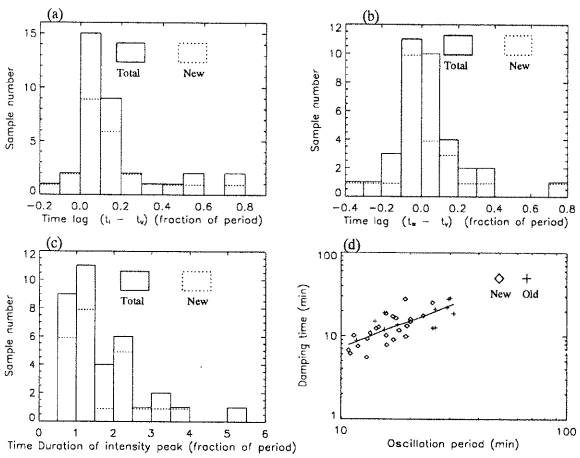

Figure 5. Histograms of the time lag of (a) the first intensity peak, and (b) the Doppler line width peak to the Maximum Doppler-shift pulse. (c) Histogram of the duration of the intensity peak above 1/e of the maximum value. The solid and dashed strips have the same meaning as in Fig. 4. (d) Scaling of the oscillation damping time with the period. Diamonds mark the new data sets obtained in 2002, and the crosses mark the old data sets obtained in 1999-2001. The solid line is the best fit scaling.

had a high cadence of 50 s, which allows a detection of short-period oscillations of ~3 min period, no oscillations are found with periods shorted than 10 min. We measure oscillation periods in the range 10.8−31.1 min with a mean of 18.5±5.8 min, damping times of 5.5−28.9 min with a mean of 14.6±6.3 min, maximum Doppler velocities of 14−315 km s^{-1} with a mean of 102±81 km s^{-1} and the derived maximum displacements of 2−54 Mm with a mean of 18±15 Mm.

Figures 5a and b indicate that the shift peaked earlier than the flux, but almost simultaneously with the line width. Figure 5c shows that the duration of intensity peak (defined as the time spent at brightness above $1/e$ of the maximum) is approximately equal to the oscillation period. In 13 of 35 oscillation components, the intensity curves have several peaks showing a non-periodic behavior (Table 1). The best fit power law scaling of the damping time with the period gives an exponent of 1.07 ± 0.16, i.e. a linear relation. In 5 cases (e.g. cases 1, 2 and 3), these events repeat at the same place and manifest similar oscillation features such as identical periods and initial Doppler shifts of the same sign. These features suggest that the recurring Doppler oscillations were related to the same magnetic structures.

sive and catastrophic energy release, and mass ejections in the overlying chromosphere and corona. The photospheric magnetic structure is essential for these processes of energy conversion and transport.

Sunrise aims to observe manifestations of small-scale magnetic structure on a spatial scale of 30–100 km (0.05 arcsec). Magnetic structures at such fine scales are seen in the simulations of Cattaneo [4], Stein and Nordlund [5] and Vögler et al. [6]. Sunrise also aims to follow their evolution on the relevant time scales, ranging from seconds (Alfvén crossing time) over roughly a day [7], to weeks in the case of sunspots.

Another aim of Sunrise is to provide simultaneous high-resolution observations of the chromospheric dynamics and brightness together with the photospheric magnetic field and velocity structure. This should enable us to determine wave modes and shock propagation, so that the transport of mechanical energy to the upper atmosphere may be quantitatively investigated. Hence, we may be able to identify the dominating heating mechanism of the chromospheric network as well as to determine the spatial distribution of hot and cool material in the chromosphere [8], [9], [10], [11] and to clarify its association with the magnetic field structure.

Such studies of small-scale magnetic concentrations afforded by Sunrise will help to uncover the physics of global solar variability, both for the total (wavelength-integrated) irradiance variations [12], [13] and for the larger variations at short wavelengths affecting the Earth's upper atmosphere (e.g. [14]).

The high-resolution and polarimetric capabilities of Sunrise should enable a test of the paradigmatic hot wall scenario of flux tube heating [15], [16]. The magnitude of the brightness variations as a function of size, inclination, and position of magnetic flux concentrations will be precisely measured [17], [18]. The direct accessibility to the UV will be able to extend such studies to the portion of the spectrum showing large variations.

Since a balloon environment allows long time series at a uniformly high resolution, Sunrise can provide information regarding the evolution of magnetic flux and the primary processes of flux emergence, recycling, magnetic reconnection, and removal from the photosphere.

The large magnetic flux emergence rates observed in the quiet solar atmosphere suggest that magnetic stresses leading to current dissipation and reconnection could be the dominant factor for coronal heating [19]. With Sunrise it could become possible to extend these measurements to the sub-arcsec range, where the emergence rates possibly increase by another two orders of magnitude due to convective flux recycling [20] or local dynamo action [4].

2. INSTRUMENT CONCEPT

The Sunrise instrumentation [21] consists of a main telescope with an aperture of 1 m, feeding three focal-plane instruments: the spectrograph-polarimeter (SP) for measurements of spectral line profiles in all 4 Stokes parameters, the filtergraph (FG) for images in selected wavelength bands, and the magnetograph (Imaging Magnetograph Experiment, IMaX) for maps of the vector magnetic field. A correlation tracker controlling a tip-tilt steering mirror provides image stabilisation and high-precision guiding.

2.1. Main Telescope

The main telescope has an aperture of 1 m and consists of a parabolic primary mirror (M1) with a focal length of 2.5 m and an elliptic secondary mirror (M2); the resulting effective focal length is 25 m (f/25). The telescope has a Gregorian configuration, with the primary image formed between the two mirrors (see Fig. 2). At this location a field stop is

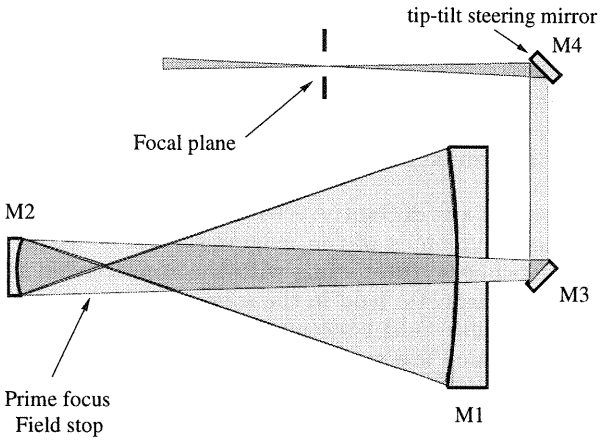

Figure 2. Optical layout of the Sunrise telescope

placed, a heat rejection cone with a central hole that defines the useable field of view, corresponding to 148 000 km on the solar surface. The field stop reflects 99% of the incoming flux out of the telescope. This reduces the heat load on the focal-plane instrumentation to about 10 W. The light passing through the field stop is reflected off M2 and folded back by the flat mirrors M3 and M4 to feed the focal-plane package. The latter (spectrograph-polarimeter, filtergraph, and magnetograph) is mounted piggy-back on the telescope structure. The tip-tilt steering mirror M4 is controlled by the correlation tracker unit and provides precise pointing and guiding. Stray light is minimized by covering the telescope structure with multi-layer insulation (MLI) from both inside and outside, by a set of baffle rings, and by a conical primary-mirror-bore baffle.

The primary mirror (M1) will be made of silicon carbide ceramic (C/SiC). The strength of this material makes extremely light-weight mirrors possible, which

retain their shape in virtually all orientations. The primary mirror and mount together weigh 65 kg. Because of C/SiC's high thermal conductivity a rather simple thermal design with passive cooling is possible. The field stop at the prime focus is also passively cooled: heat absorbed by the field stop is removed by heat pipes to a radiator mounted on the instrument structure.

The 45 degree reflections by M3 and M4 introduce a constant instrumental polarisation, which leads to a crosstalk between the Stokes parameters (the polarization analyzers are placed after the secondary focus). This effect will be calibrated on the ground, so that the polarisation data can be corrected accordingly.

2.2. Pointing and Precision Guiding

Meeting the requirement of very high spatial resolution down to 0.05 arcsec implies a substantial effort to accurately point and guide the telescope. Fluctuations of the index of refraction due to atmospheric turbulence (the main reason for image deterioration in ground-based observations) are negligible at balloon altitudes of 40 km, but image motions due to the operation of the various mechanisms and motors in the gondola, the telescope, and the instruments, as well as the swinging of the gondola must be compensated down to a level of about 0.01 arcsec. In order to reach this goal, the pointing and guiding system of Sunrise works on two levels:

a) solar pointing of gondola/telescope in azimuth by a torque motor drive as part of the momentum transfer unit (MTU) at the gondola support point; pointing in elevation by tilting the telescope, and

b) precision guiding and compensation of image motion. The guiding is performed in a closed-loop servo system that consists of a correlation tracker (CT) to provide the error signal and the piezo-driven steering mirror M4 performing the correction.

2.3. Wavefront Control System

Because of the large temperature differences between ground and flight conditions it is important to have reliable and accurate in-flight alignment capabilities. To this end a wavefront control system is envisaged that is capable of detecting low-order modes of wavefront deformations in the telescope. A wavefront sensor measures the actual state of the optical alignment and generates an appropriate error signal. A control system converts this error signal into actuation signals which are used to drive the position of the secondary mirror, M2, and the tip-tilt mirror, M4.

The detection principle is based on a correlation tracker generating tip and tilt error signals. However, instead of sensing the position of a single image derived from the entire pupil of the telescope, seven subapertures sense the local wavefront tilt in two zones of the pupil. The information derived from the seven independently analysed images of the same solar scene suffices to determine the coefficients of a Zernike function decomposition of the wavefront error up to the third radial degree. The coefficients for tip and tilt, defocus, and Seidel coma are used as error signals for the control system. The system is able to measure and compensate axial and lateral displacement of the secondary mirror, M2, as well as dynamic image displacement errors.

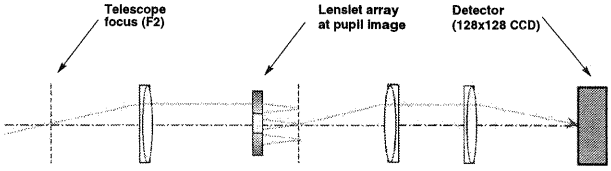

Figure 3. Optical configuration of wavefront sensor

Fig. 3 shows a sketch of the wavefront sensor, which is located in the vicinity of the secondary focus. The sensor consists of a collimating lens, a hexagonal lenslet array with seven – one central and six peripheral – elements covering the pupil of the telescope, and lenses that reimage the lenslet array focal plane onto a matrix array detector (CCD camera).

2.4. Spectrograph-Polarimeter

The achievement of the main science goals of Sunrise depends on quantitative and accurate measurements of the strength and orientation of the magnetic field with appropriate spatial, spectral, and temporal resolution. The spectrograph-polarimeter (SP) combines high-resolution vector-polarimetry with a multi-line Echelle spectrograph, simultaneously providing photospheric magnetic field measurements (polarimetric branch) and diagnostic spectroscopy of photospheric and chromospheric lines (diagnostic branch). The SP is based on an all-mirror scanning Echelle spectrograph in a modified Littrow configuration. A preliminary schematic view of the Spectrograph-Polarimeter is shown in Fig. 4. Apart from the UV capability, the SP is similar to the POLIS instrument now installed at the VTT on Tenerife [23].

The polarimetric branch of the SP is dedicated to the determination of the magnetic field vector in the solar photosphere. This is carried out by measuring the full Stokes vector using the pair of Fe I lines at 630.2 nm. The 630.25 nm line is one of the most Zeeman-sensitive lines in the visible spectrum (Zeeman triplet with a Landé factor of 2.5), thus providing large Stokes signals. The design of the polarimetry unit draws upon the heritage of the Advanced Stokes Polarimeter [22], which has been very

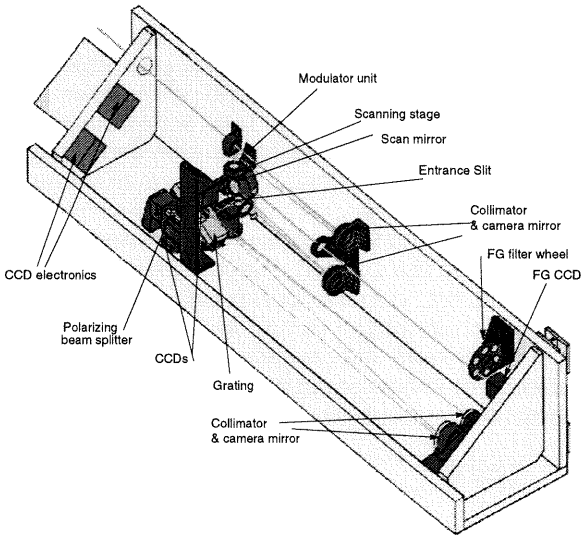

Figure 4. Perspective view of spectrograph-polarimeter and filtergraph in their common enclosure. The light enters from the rear. The modulator unit consists of a waveplate mounted in a rotary stage and a precision encoder to synchronize the CCD cameras.

successfully used for ground-based observations, and the spectro-polarimeter for the FPP instrument on Solar-B. The polarimetry unit is a dual beam system with a rotating modulator and a polarizing beam splitter mounted in front of the corresponding CCD.

The diagnostic branch of the SP measures the intensity profile of a spectral line that is chosen from a number of preselected lines by way of a set of narrow-band filters mounted on a filter wheel. With Sunrise, the observable wavelength range extends well into the UV, down to 200 nm. In principle, this permits spectroscopy of the Mg II k line core at 279.6 nm, an excellent diagnostic of the chromosphere.

2.5. Filtergraph

The filtergraph (FG) is realized as a multi-wavelength slit-jaw camera of the spectrograph-polarimeter (see Fig. 4). This allows both instruments to receive the full amount of light in all wavelengths. In addition, the image of the spectrograph entrance slit in the filtergrams allows a precise identification of the region simultaneously observed with the SP.

Three wavelengths each are chosen to sample the photosphere and the chromosphere. The 205 nm continuum allows studies of the upper photosphere at a spatial resolution of 0.05 arcsec (35 km on the Sun). At the same time this wavelength is important for the stratospheric ozone household. The CN-band at 388 nm provides the highest contrast, and thus sensitivity to thermal inhomogeneities, in the photosphere. The continuum radiation at 550 nm samples the deep layers of the photosphere. The chromospheric wavelength bands center on strong spectral lines: Mg II k (279 nm), Ca II K (393 nm), and Mg I (285 nm). Each of these lines samples the chromospheric height range and thermal structure in a different way. In order to ensure diffraction limited images at even the shortest wavelengths, we propose to carry out a phase diversity reconstruction of the images. An appropriate optical element will be introduced into the imager.

2.6. Magnetograph (IMaX)

The Imaging Magnetograph Experiment for Sunrise (IMaX) is an imaging vector magnetograph based upon narrow-band filters. The instrument will provide fast-cadence two-dimensional maps of the complete magnetic vector and the line-of-sight velocity with high spatial resolution. The optical scheme of the magnetograph is shown in Fig. 5.

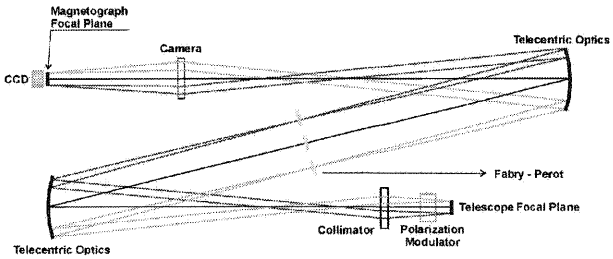

Figure 5. Optical scheme of the magnetograph.

IMaX images will be taken in two narrow wavelength bands in either wing of a photospheric spectral line. Wavelength selection will be made by using a tunable system of Fabry-Perot etalons in a telecentric path. In this way, one ensures the homogeneity of the selected wavelength over the field of view.

For the modulation of the polarization signals, a unit based on liquid crystals is currently being considered [24]. The main advantage is that no rotating parts are needed.

3. BALLOON CONCEPT

The Sunrise telescope is mounted on the elevation axis to a frame consisting of standard aluminium components. It is designed to withstand the vertical acceleration that is applied to the attachment rings when the parachute is opened near the termination of the flight. This structure and aeroflex shock absorbers protect the payload from the vertical and horizontal components of the landing shock load in case of landing in cross winds. The gondola can be moved in azimuthal direction to point the telescope and the solar panels towards the Sun. This is realized by means of a momentum transfer unit (MTU) mounted at the top of the gondola. The telescope deployed in the gondola is shown in Fig. 6.

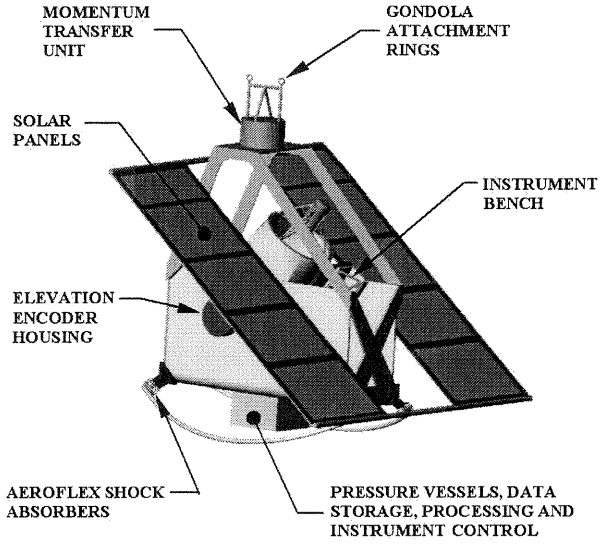

Figure 6. Sunrise telescope assembled in the balloon gondola: operation mode. During ascent, descent, and landing the telescope is stowed horizontally, so that it is protected by the 'cradle'. The gondola is suspended from the main telescope frame and rotates with its structure while the telescope is being driven directly via the MTU, which will be designed to minimize jitter in pointing stability.

Sunrise will be flown in the framework of NASA's LDB (Long Duration Balloon) program. We plan a flight of 10-12 days during a southern hemisphere summer from the ballooning facilities at McMurdo (Antarctica, 77.86 south latitude, 167.13 deg east longitude). The flight trajectory is circumpolar, bounded between 72 deg and 83 deg south latitude. Float altitudes are 35–40 km. Flying during summer over Antarctica has the advantage of permanent sunlight and small elevation changes of the Sun, so that observation and power generation are uninterrupted; furthermore, the thermal conditions do not vary significantly and the balloon floats at nearly constant altitude. These advantages more than compensate for the logistical difficulties associated with campaigns in Antarctica.

4. REFERENCES

1. Parker E.N., *Astrophysical Journal*, 407, 342, 1993.

2. Huang, P., Musielak, Z. E., Ulmschneider, P., *Astronomy and Astrophysics*, 297, 579, 1995.

3. Ulmschneider, P., Musielak Z. E., *Astronomy and Astrophysics*, 338, 311, 1998.

4. Cattaneo F., *Astrophysical Journal*, 515, L39, 1999.

5. Stein R.F., Nordlund Å, these proceedings, 2002.

6. Vögler A. et al., in preparation, 2002.

7. Hagenaar H.J., *Astrophysical Journal*, 555, 448, 2001.

8. Ayres T.R., Testerman L., Brault J.W., *Astrophysical Journal*, 304, 542, 1986.

9. Solanki S.K., Livingston W., Ayres T., *Science*, 263, 64, 1994.

10. Uitenbroek H., Noyes R.W., Rabin D., *Astrophysical Journal*, 432, L67, 1994.

11. Carlsson M., these proceedings, 2002.

12. Fröhlich C., *Space Science Reviews*, 94, 15, 2000.

13. Fligge M. et al., *The Solar Cycle and Terrestrial Climate*, ed. A. Wilson, ESA SP-463, p. 117, 2000.

14. Solanki S.K., Fligge M., Unruh Y.C., *Recent Insights into the Physics of the Sun and Heliosphere - Highlights from SOHO and Other Space Missions*, eds. P. Brekke, B. Fleck, and J.B. Gurman, IAU Symposium, No. 203, p. 66, 2001.

15. Spruit H.C., *Solar Physics*, 50, 269, 1976.

16. Deinzer W., Hensler G., Schüssler M., Weisshaar E., *Astronomy and Astrophysics*, 139, 426, 1984.

17. Spruit H.C., Zwaan C., *Solar Physics*, 70, 207, 1981.

18. Steiner O., Grossmann-Doerth U., Knölker M., Schüssler M., *Solar Physics*, 164, 223, 1996.

19. Schrijver C.J. et al., *Nature*, 394, 152, 1998.

20. Ploner S.R.O., Schüssler M., Solanki S.K., Gadun A.S., *Advanced Solar Polarimetry — Theory, Observation and Instrumentation*, ed. M. Sigwarth, ASP Conference Series, Vol. 236, p. 363, 2001.

21. Schmidt W. et al. *Astronomische Nachrichten*, 322, 363, 2001.

22. Elmore D.F., Lites B.W., Tomczyk et al., *Proceedings SPIE*, 1746, 22, 1992.

23. Schmidt W., Kentischer T., Bruls J., Lites B.: *Advanced Solar Polarimetry — Theory, Observation and Instrumentation*, ed. M. Sigwarth, ASP Conference Series, Vol. 236, p. 49, 2001

24. Del Toro Iniesta J.C., Martínez Pillet V., González Escalera V., *Advances in the Physics of Sunspots*, eds. B. Schmieder, J.C. del Toro Iniesta, M. Vázquez, ASP Conference Series, Vol. 118, p. 356, 1997.